

Part of Special Issue on  
Semiconductor Spintronics

# Toward combined transport and optical studies of the 0.7-anomaly in a quantum point contact

Enrico Schubert<sup>1,1</sup>, Jan Heyder<sup>1,2</sup>, Florian Bauer<sup>1,2</sup>, Bernd Waschneck<sup>1</sup>, Wolfgang Stumpf<sup>3</sup>, Werner Wegscheider<sup>3</sup>, Jan von Delft<sup>1,2</sup>, Stefan Ludwig<sup>1</sup>, and Alexander Högele<sup>1</sup>

<sup>1</sup> Center for NanoScience and Department of Physics, Ludwig-Maximilians-Universität München, Geschwister-Scholl-Platz 1, 80539 München, Germany

<sup>2</sup> Arnold Sommerfeld Center for Theoretical Physics, Ludwig-Maximilians-Universität München, Theresienstrasse 37, 80333 München, Germany

<sup>3</sup> Laboratory for Solid State Physics, ETH Zurich, 8093 Zurich, Switzerland

Received 18 September 2013, revised 14 February 2014, accepted 5 March 2014

Published online 12 April 2014

**Keywords** 0.7-anomaly, optical spectroscopy, quantum point contacts, two-dimensional electron systems

\* Corresponding author: e-mail enrico.schubert@physik.uni-muenchen.de, Phone: +49 89 2180 3349, Fax: +49 89 2180 3182



This is an open access article under the terms of the Creative Commons Attribution License, which permits use, distribution and reproduction in any medium, provided the original work is properly cited.

A quantum point contact (QPC) causes a one-dimensional constriction on the spatial potential landscape of a two-dimensional electron system. By tuning the voltage applied on the QPC gates which form the constriction at low temperatures the resulting regular step-like electron conductance quantization can show an additional kink near pinch-off around  $0.7(2e^2/h)$ , called 0.7-anomaly. In a recent publication, we presented a combination of theoretical calculations and transport measurements that lead to a detailed understanding of the microscopic origin of the 0.7-anomaly. Functional renormalization group-based calculations were performed exhibiting the 0.7-anomaly even when no symmetry-breaking external magnetic fields are involved.

According to the calculations the electron spin susceptibility is enhanced within a QPC that is tuned in the region of the 0.7-anomaly. Moderate externally applied magnetic fields impose a corresponding enhancement in the spin magnetization. In principle, it should be possible to map out this spin distribution optically by means of the Faraday rotation technique. Here we report the initial steps of an experimental project aimed at realizing such measurements. Simulations were performed for a heterostructure designed to combine transport and optical studies. Based on the simulation results a sample was built and its basic transport and optical properties were investigated.

**1 Introduction** A quantum point contact (QPC) is a short, one-dimensional constriction usually realized within a two-dimensional electron system (2DES), by applying voltage to metallic gates, thereby depleting the electrons beneath and only leaving a narrow transport channel whose width can be tuned by the applied gate voltage. When a QPC is opened up by changing the applied gate voltage, its conductance rises in integer steps of the conductance quantum,  $G_Q = 2e^2/h$  [1–3], but also shows a shoulder-like intermediate step at the onset of the first plateau around  $\simeq 0.7G_Q$ . This phenomenon, known as the 0.7-anomaly, has a very intriguing dependence on temperature ( $T$ ), magnetic field ( $B$ ), and source–drain voltage ( $V_{SD}$ ) [4–7]. A summary of the status of

various previous theoretical treatments thereof may be found in [8].

In a recent publication [9], we presented a combination of theoretical calculations and transport measurements that lead to a detailed understanding of the microscopic origin of the 0.7-anomaly. The anomaly is caused by a smeared van Hove peak in the local density of states (LDOS), whose weight, shape, and position depends on sample geometry (width, length, and shape of the QPC confinement potential). The van Hove peak enhances the effect of interaction by two main mechanisms: first, it enhances the effective Hartree barrier, and thus the elastic back-scattering due to Coulomb repulsion; second, it opens up a phase space for inelastic scattering

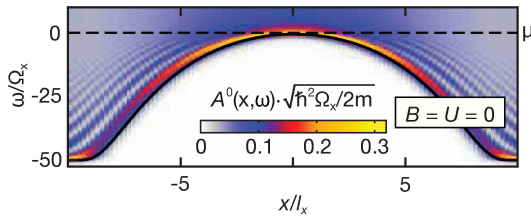


**Figure 1** The bare local density of states,  $A^0(x, \omega)$ , in the central region of the QPC as a function of position  $x$  and energy  $\omega$ . The maximum of  $A^0$  follows the shape of the band, i.e., the shape of the applied potential, resulting in a distinct ridge-like structure (yellow), the van Hove ridge.

which is enhanced further by increasing the temperature or the source–drain bias voltage.

The present paper serves two purposes. First, in Section 2 we summarize some of the main results from [9], highlighting, in particular, one of its central predictions: the local spin susceptibility is predicted to be anomalously enhanced in the vicinity of the QPC. Second, in Section 3 we describe the initial stages of an experimental project that ultimately aims at detecting the predicted anomalous behavior of the spin susceptibility in a QPC by optical methods.

**2 Microscopic origin of the 0.7-anomaly** In experiments, QPCs are commonly defined using the field effect to create an electrostatic saddle point potential (see, e.g., Ref. [9], Fig. 1). To model this effective 1D constriction we use a strict 1D-barrier along the electronic transport direction  $x$ . We choose the potential,  $V(x)$ , to be symmetric around  $x = 0$  and parabolic near the top,

$$V(x) = \tilde{V}_c + \mu - \frac{m}{2\hbar^2} \Omega_x^2 x^2, \quad (1)$$

where  $\hbar$  is Planck’s constant and  $m$  the effective electron mass. The barrier height is governed by  $\tilde{V}_c$ , which mimics the role of gate voltage in experiment; it is chosen such that for  $\tilde{V}_c = 0$ , the barrier top lies at the chemical potential  $\mu$ . The barrier curvature  $\Omega_x$  defines the effective length of the QPC, which is proportional to  $l_x = \sqrt{\hbar^2 / (2m\Omega_x)}$  (see [10] and supplementary information of [9] for more details). Figure. 1 shows the bare LDOS,  $A^0(x, \omega)$ , of the QPC as a function of position  $x$  and energy  $\omega$  (measured relative to  $\mu$ ). The LDOS has a maximum right above the potential  $V(x)$  (black thick line), visible as a yellow-red structure. This structure, which lies at the heart of the explanation for the 0.7-anomaly, will be called a “van Hove ridge.” Near the barrier center the ridge maximum lies slightly higher in energy than the potential  $V(x)$ , by an amount that scales like the barrier curvature  $\Omega_x$ .

To theoretically investigate the influence of magnetic field and interactions, we study a one-dimensional tight-binding chain with lattice spacing  $a$ , an onsite energy given by a discretized version of the potential (1), a local Zeeman energy  $-\sigma B/2$  (thus  $B$  denotes  $g$ -factor times magnetic field), and a purely local (onsite) interaction  $U$ . The effective strength of interaction effects scales as  $U/U_c$ , where

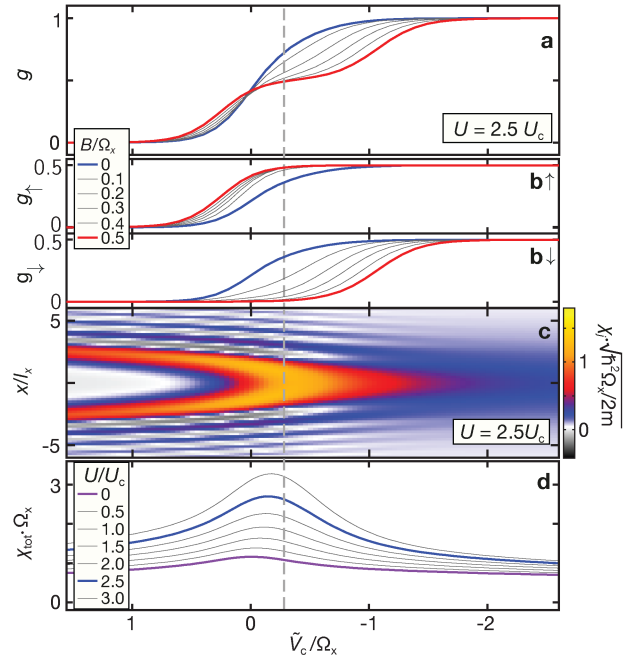


**Figure 2** (a) Calculated linear conductance  $g(V_c)$  as a function of barrier height for several values of magnetic field, at zero temperature. Interactions cause a weak shoulder even at zero field, which strengthens for intermediate fields and eventually develops into a spin-resolved conductance step at high field. (b $\uparrow$ /b $\downarrow$ ) Calculated spin-resolved conductance curves for the same magnetic fields as in (a). The conductance curves for spin-up and spin-down react in an asymmetric fashion on an applied field: a combination of Pauli exclusion principle and Coulomb blockade (Hartree effect) leads to a strong reduction of  $\downarrow$ -conductance, resulting in the phenomenon of the 0.7-anomaly. (c) Local spin susceptibility,  $\chi(x, \tilde{V}_c)$ , as a function of position  $x$  and barrier height  $\tilde{V}_c$  for a fixed value of interaction strength,  $U = 2.5 U_c$ . The strongest response of the system to a small applied magnetic field happens in the center of the barrier and coincides with the barrier height for which the 0.7-anomaly occurs (see (a)), highlighted with the gray dashed vertical line around  $\tilde{V}_c = -0.25\Omega_x$ . (d) The total spin-susceptibility of the QPC,  $\chi_{\text{tot}}$ , for several values of interaction strength.

$U_c = \sqrt{\hbar^2 \Omega_x / (2ma^2)}$  is inversely proportional to  $A_{\text{max}}^0$ , the height of the van Hove ridge at the barrier center (for details see [10]). For this model we calculated the linear conductance and the local density and magnetization per site at zero temperature, incorporating interaction effects using the functional Renormalization Group (fRG) [9–14].

Figure 2a shows the calculated  $\tilde{V}_c$ -dependence of the linear conductance  $g = G/G_Q$  of the lowest mode of a QPC for several values of magnetic field and a finite interaction strength. We find very good qualitative agreement with measured curves (see, e.g. [9]) not only for zero field, where the asymmetry of the step becomes manifest in a weak shoulder (marked by gray dashed vertical line), but also at finite field, where the single step develops via a 0.7-anomaly into a double step of width  $g_{\text{eff}} \mu_B B$ . Figure 2b $\uparrow$  and Fig. 2b $\downarrow$  show the calculated spin-resolved conductance for the same fields and interaction used in Fig. 2a. As expected, the conductance

increases/decreases for the favored/disfavored (spin-up/spin-down) electrons. But unlike in the non-interacting case (not shown) the spin-down step is shifted much more strongly toward negative values of  $\tilde{V}_c$  than the spin-up shift is shifted toward positive values of  $\tilde{V}_c$ . This can be explained as follows: Once a finite field breaks spin-symmetry, interactions push away spin-down electron out of the QPC's center, thereby depleting their density around the barriers top and consequently strongly reducing their probability of transmission. The 0.7-anomaly at finite magnetic field is a natural consequence of this interaction-induced asymmetry.

As explained in detail in Ref. [9], the origin of the 0.7-anomaly is caused by the presence of the van Hove ridge in the LDOS. Its apex crosses the chemical potential, when the QPC is tuned into the sub-open regime, that is, when the conductance takes values  $0.5 \lesssim g \lesssim 1$ . As a consequence, the local spin-susceptibility,  $\chi(x) = \frac{1}{2} (\partial_h m(x))_{h=0}$ , shows not only a strong spatial dependence due to the inhomogeneity of the QPC, but also a strong  $\tilde{V}_c$ -dependence, when the potential is shifted through  $\mu$  (see Fig. 2c). This also manifests itself in the total spin-susceptibility of the QPC,  $\chi_{\text{tot}} = \int_{x \in \text{QPC}} dx \chi(x)$ , which is plotted in Fig. 2d for several values of interaction strength. Three direct consequences of interactions stand out: First, interactions strongly enhance the effect of an applied magnetic field. Second, the maximum in the QPC's susceptibility is shifted to somewhat lower values of  $\tilde{V}_c$  and, third, this maximum occurs when the QPC is sub-open (gray dashed vertical line in Fig. 2, compare with conductance curves in Fig. 2a). These anomalous spatial structures in the spin susceptibility serve as the main incentive for the experimental work described further below, whose ultimate goal is to detect these structures by opto-transport hybrid measurements.

**3 Motivation for the experiment** Next, we describe ongoing experimental work, whose ultimate goal is to test the following prediction emerging from the theoretical work described above: For a QPC tuned in the regime of the 0.7-anomaly at zero external magnetic field, theory predicts an enhancement in the local electron spin susceptibility [9]. At finite magnetic fields the enhanced spin susceptibility should give rise to electron-spin polarization with a spatial distribution characteristic of a QPC operated at the point of the 0.7-anomaly (see Fig. 2a). Moreover, this polarization would also result in spin-sensitive conductance. In principle, both signatures could be probed by optical means: while spatially-resolved Kerr or Faraday rotation could be used to map out the local spin-polarization in the vicinity of the QPC, polarization-selective optical spin-injection could be exploited to create an electron-spin imbalance across the QPC to drive spin-polarized currents. Our first step en-route to combined transport and optical spectroscopy of a QPC in the 0.7-anomaly regime was to design a heterostructure that would allow to implement both spin-sensitive Faraday rotation and spin-selective charge carrier injection.

The following experimental part is divided into three sections. In Section 3.1 we discuss the optimization process of the heterostructure design and the results of the simulations

performed with *nextnano3* [15]. In Section 3.2 we present initial transport and optical characterization measurements of the heterostructure. Section 3.3 describes the present stage of our experiments and provides perspectives for the combined transport and optical spectroscopy of the 0.7-anomaly in a QPC.

### 3.1 Semiconductor heterostructure design and simulations

The design of the heterostructure for combined transport and optical experiments was guided by two main objectives. On one hand, we intended to realize a high quality two-dimensional electron system (2DES) suited for the observation of the 0.7-anomaly in a QPC. On the other hand, the sample structure should be designed to allow for spin-selective optical excitations of charge carriers from the valence band into the conduction band states of the 2DES just above the Fermi level, and at the same time avoid excitations of charge carriers in any other heterostructure layer. To make all sample regions but the 2DES transparent to light at optical frequencies that meet the resonance condition for interband excitation of electrons into the Fermi sea we chose to embed an  $\text{In}_x\text{Ga}_{(1-x)}\text{As}$  quantum well (QW) hosting the 2DES in higher bandgap materials such as GaAs and AlGaAs. Accordingly, optical excitations from the valence band states into the conduction band states within the  $\text{In}_x\text{Ga}_{(1-x)}\text{As}$  QW exhibit the smallest energy for interband transitions, provided that the concentration  $x$  of indium is finite. At the same time quantum confinement associated with the QW removes the degeneracy of heavy- and light-hole subbands at the  $\Gamma$ -point of bulk zinc blende semiconductors, which in turn ensures "clean" dipolar selection rules for spin-selective optical excitations from the heavy hole subband at  $E_{\text{hh}}$  into the states at  $E_F$  of the 2DES.

Figure 3 illustrates the basic layout of our heterostructure. The corresponding layer sequence along the sample growth direction is shown in the left panel of Fig. 3. The  $\text{In}_x\text{Ga}_{(1-x)}\text{As}$  QW of variable thickness  $z_{\text{QW}}$  and an indium fraction  $x$  in the range of  $0 < x < 0.1$  is sandwiched between GaAs and  $\text{Al}_{0.235}\text{Ga}_{0.765}\text{As}$  that contains a  $\delta$ -doping region located at a distance  $z_\delta$  above the QW. The AlGaAs layer acts as a tunnelling barrier between the 2DES and the semitransparent Schottky gate deposited on top of the heterostructure. The overall thickness of the AlGaAs barrier was set to half of the wavelength of the expected QW interband transition to minimize optical interference effects. The silicon  $\delta$ -doping provides excess electrons to form a 2DES inside the QW and the final GaAs top cap layer prevents oxidization of the AlGaAs barrier. In the right panel of Fig. 3 the corresponding band structure profile calculated with *nextnano3* is shown for zero external gate voltage,  $V_t = 0$ , and  $x = 0.07$ ,  $z_{\text{QW}} = 10$  and  $z_\delta = 50$  nm. The band profile bending is due to the built-in Schottky potential, accounting for the lowest QW electron level  $E_c$  to lie below the Fermi energy, in accord with our intention to create a modulation-doped 2DES within the InGaAs QW.

We recall the main properties of the intended heterostructure. First the QW containing the 2DES should exhibit the

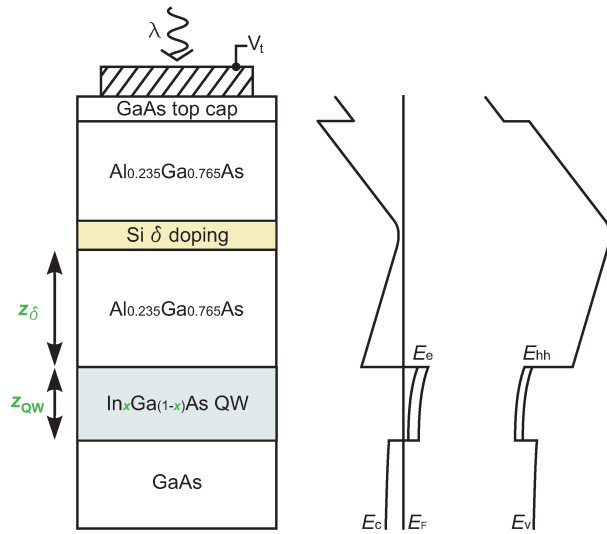


**Figure 3** Left: Schematic design of the heterostructure. It consists of a GaAs substrate on which an InGaAs quantum well (blue), AlGaAs spacer with a Si  $\delta$ -doping layer (yellow), and a GaAs cap are grown. The 2DES formed in the InGaAs quantum well is populated by electron transfer from the  $\delta$ -doping layer. A GaAs top cap layer terminates the heterostructure. A semitransparent metal gate on top of the heterostructure gives rise to a built-in Schottky potential and allows to further bend the band structure via a voltage  $V_t$ . The quantum well thickness  $z_{QW}$ , the indium concentration  $x$  and the distance  $z_\delta$  from the quantum well and the  $\delta$ -doping region were used as optimization parameters in simulations with *nextnano3*. Right: Band structure profile along the heterostructure growth direction obtained from simulations for  $V_t = 0$ .  $E_c$  and  $E_v$  denote the conduction and valance band edges,  $E_e$  and  $E_{hh}$  the lowest electron and heavy-hole levels confined in the quantum well, and  $E_F$  is the Fermi energy, respectively.

smallest interband transition energy with well defined dipolar selection rules for spin-selective excitations. Second the semiconductor matrix above and below the QW should be transparent at the intended optical frequencies. Both criteria can be satisfied by the heterostructure layout of Fig. 3. Finally, the density of the 2DES should be at least  $2 \times 10^{11} \text{ cm}^{-2}$  to ensure the required transport characteristics.

To this end we used *nextnano3* to monitor the 2DES density as a function of the optimization parameters  $x$ ,  $z_{QW}$  and  $z_\delta$ . The objective was to achieve a maximum electron density inside the QW of about  $3 \times 10^{11} \text{ cm}^{-2}$ . Simultaneously the interband transition wavelength of the QW region, which follows from the energy difference between the lowest QW hole level and the Fermi energy, was intended to lie above 830 nm in order to not overlap with optical transitions of carbon impurities [16] inherent to the molecular beam epitaxy (MBE) growth process of the heterostructure. In Fig. 3 these adjustable parameters for the simulations are highlighted in green. Raising the QW thickness  $z_{QW}$  as well as the QW indium content  $x$  mainly increases the QW interband transition wavelength. Reducing the distance  $z_\delta$  between the QW and the  $\delta$ -doping

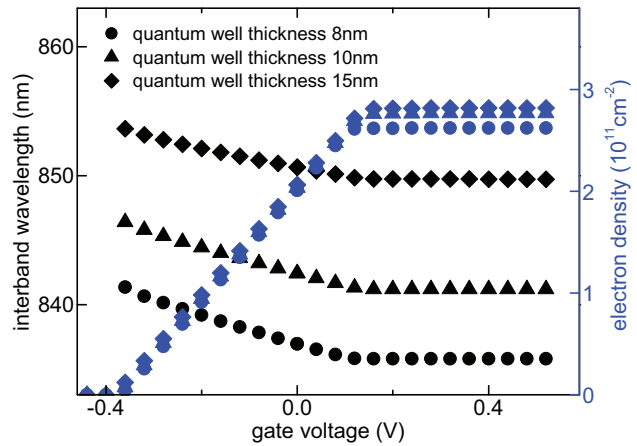


**Figure 4** Simulation results for the QW electron density (blue) and the interband transition wavelength (black) as a function of gate voltage. Results are shown for three different QW thicknesses of  $z_{QW} = 8$  nm (circles), 10 nm (triangles), and 15 nm (squares) for a fixed indium content of  $x = 0.07$  and a fixed spacer distance between the doping region and the QW of  $z_\delta = 50$  nm.

layer tends to increase the 2DES density. However, at small QW thickness, proximity of the QW 2DES and the doping layer, and a high indium concentration typically reduce the mobility of the QW electrons and should be avoided.

Figure 4 shows the simulation results for three different heterostructures with an indium concentration of  $x = 0.07$  and  $z_{QW} = 50$  nm. The QW thickness was taken as 8, 10, and 15 nm to obtain a variation in the QW electron density (blue) and the interband transition wavelength (black) as a function of the voltage applied to the semitransparent top gate. Decreasing the gate voltage increases the energy of the QW electron levels with respect to the Fermi energy which gradually depletes the 2DES density inside the QW. This depletion becomes increasingly pronounced below gate voltages of 0.15 V until the pinch-off is reached at about  $-0.4$  V for all three heterostructures. The interband wavelength remains constant for  $V_t > 0.25$  V. At more negative gate voltages the simulations predict a redshift of the resonance condition that is associated with a decrease of the Fermi energy. In Fig. 4 the maximum 2DES density as well as the optical transition wavelength are close to our intended values.

### 3.2 Basic transport and optical characteristics

Based on these simulation results a heterostructure was grown by MBE with an indium concentration of  $x = 0.07$ , the separation between the QW and the  $\delta$ -doping layer of  $z_{QW} = 50$  nm, and a QW thickness of 10 nm (compare Fig. 3). Subsequently the sample material was characterized with respect to basic transport and optical properties. To determine the electron density and mobility of the 2DES a standard Hall bar geometry was used. The Hall bar mesa was fabricated by conventional wet etching techniques and AuGe/Ni/AuGe Ohmic contacts were defined as Ohmic contacts to the 2DES. To allow control of the electron density a semitransparent titanium gate with a thickness of 5 nm

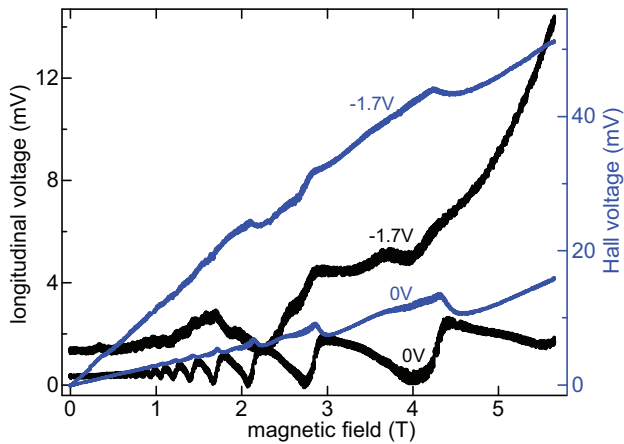


**Figure 5** Measured longitudinal (black) and Hall voltages (blue) as a function of the perpendicularly applied magnetic field at top gate voltages of 0 V and  $-1.7$  V ( $T = 4.2$  K). Distortions of the Hall voltage between plateaus are due to an asymmetry of the used Hall bar geometry which gives rise to an Ohmic resistance contribution to the Hall voltage.

was deposited on top of the central region of the Hall bar structure.

The electron density and mobility were extracted from four-terminal dc Hall voltage measurements before the sample was subjected to light. Magnetic fields of up to 5.7 T were applied perpendicularly to the QW plane. By fitting the Hall voltage  $U_{xy}$  versus the applied magnetic field  $B$  in the linear regime at low  $B$  (Fig. 5) the carrier density of the 2DES is extracted by

$$n_{2DES} = \frac{I}{e \cdot dU_{xy}/dB}. \quad (2)$$

$e$  is the elementary charge and  $I$  is the current through the Hall bar. The mobility  $\mu_{2DES}$  of the electron system inside the QW was obtained from the longitudinal voltage at zero magnetic field  $U_{xx}(B = 0)$  (Fig. 5) using the relation

$$\mu_{2DES} = \frac{0.75}{e \cdot n_{2DES} \cdot U_{xx}(B = 0)} \quad (3)$$

and the electron density  $n_{2DES}$  obtained according to Eq. (2). The number in the numerator is a scaling factor imposed by the particular geometry of the employed Hall bar structure. The same procedure was also carried out after broad-band illumination of the sample.

In a second step we studied basic optical properties of the sample by investigating the photoluminescence (PL) from the Hall bar. A cryogenic confocal microscope with an optical spot size of 1  $\mu\text{m}$  was used to record the local PL response, which was then spectrally dispersed by a monochromator and detected with a low-noise liquid nitrogen cooled CCD. All measurements were carried out at a sample temperature of 4.2 K.

The combined transport and optical characterization results are shown in Fig. 6. The interband transition wavelength (black) and the QW electron density (blue) are shown

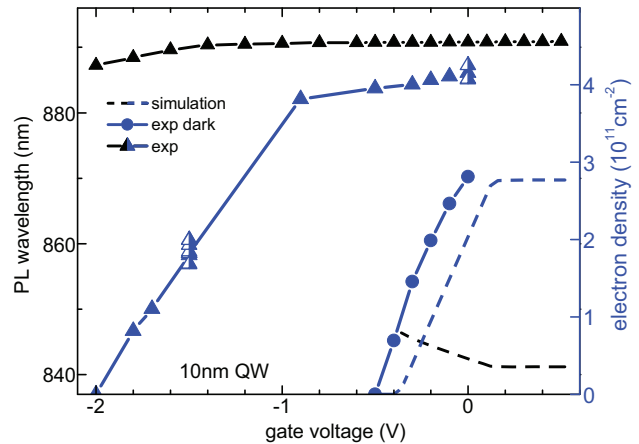


**Figure 6** Transport and optical characterization of the heterostructure. Data (symbols; lines are guides to the eye) and corresponding simulations as in Fig. 4 (dashed lines) for a heterostructure with a QW of thickness  $z_{QW} = 10$  nm, 7% of indium concentration, and  $z_{\delta} = 50$  nm. The wavelength of the photoluminescence peak maximum and the electron density of the QW 2DES are shown as a function of gate voltage in black and blue, respectively. Circles and triangles indicate the measurement results before and after light illumination of the Hall bar, respectively. Half-filled triangles correspond to electron densities measured after repeated illumination of the sample. The photoluminescence was obtained from the central region of the Hall bar using a confocal setup with excitation powers of 7  $\mu\text{W}$  in the range of  $+0.6$  to  $-1.0$  V and 0.3  $\mu\text{W}$  below  $-1.0$  V at an excitation wavelength of 830 nm. The 2DES density was derived from standard Hall measurements. All measurements were carried out at 4.2 K.

as a function of gate voltage. Circles (triangles) indicate the results of measurements done before (after) illumination of the sample with continuous wave (cw) lasers (with 815 and 830 nm center wavelength). Dashed lines show the corresponding simulation results from Fig. 4 for comparison. In the simulations all silicon dopants were assumed to be ionized, which is realized experimentally by sample illumination. Despite an increase by  $\sim 30\%$  of the 2DES density to around  $4.2 \times 10^{11} \text{ cm}^{-2}$ , upon illumination, the simulated and experimental results are in very good agreement with the predictions of the simulation. Consistently, the pinch-off gate voltage where the carrier density goes to zero is shifted to more negative values upon illumination as compared to the simulated pinch-off voltage. Repeated illumination of the sample did not introduce further significant changes in the 2DES density (half-filled triangles in Fig. 6), indicating a long-term stability of the 2DES density after the initial ionization of silicon dopants. The mobility of the 2DES was determined to be  $\sim 70,000 \text{ cm}^2 \text{ V}^{-1} \text{ s}^{-1}$  within the entire gate voltage range above  $-1.5$  V after sample illumination (data not shown).

Despite good agreement between simulations and experiment for the 2DES density, we found considerable discrepancy between expected and observed values for the wavelength of the optical transition that we monitored via PL. Figure 6 shows the wavelength of the PL peak as a function

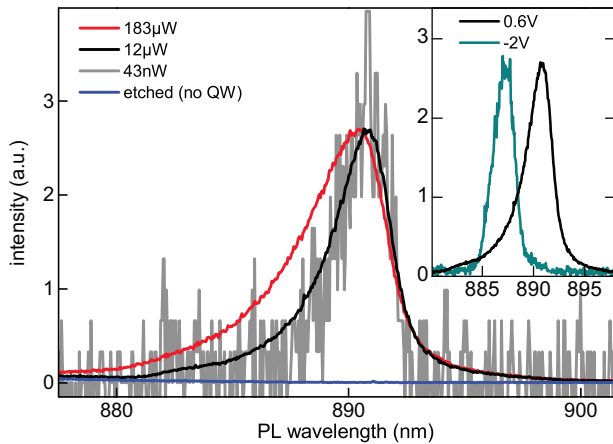


**Figure 7** Photoluminescence spectra recorded for a Hall bar sample at 4.2 K with a QW thickness of 10 nm and incident excitation powers of  $P_{\text{exc}} = 183 \mu\text{W}$  (red),  $12 \mu\text{W}$  (black, main, and inset graph) and  $43 \text{ nW}$  (gray) scaled to maximum intensity values. The photoluminescence spectra were measured in the central Hall bar region at gate voltages of  $V_i = +0.6 \text{ V}$  (flatband) under cw excitation at a wavelength of 830 nm. The photoluminescence from an area where the QW was etched away is shown in blue for reference. Inset: photoluminescence spectra at two different gate voltages of  $+0.6 \text{ V}$  (black) and  $-2.0 \text{ V}$  (green) for incident excitation power of  $300 \text{ nW}$ .

of gate voltage recorded near the center of the Hall bar. Incident laser excitation powers were  $7 \mu\text{W}$  in the voltage range between  $+0.6$  and  $-1.0 \text{ V}$  and  $0.3 \mu\text{W}$  below  $-1.0 \text{ V}$ , respectively. The excitation wavelength was set to 830 nm, close to the wavelength region of carbon impurity states in GaAs at 4.2 K [16]. The mean difference between the simulated and the measured optical transition wavelength is about 50 nm (83 meV) and a reversed energy dispersion as a function of gate voltage is observed (redshift in experiment vs. blueshift in simulations for increasing electron density). We speculate that the discrepancy partially arises from excitonic effects and the quantum confined Stark effect that were not accounted for in our simulations. Nevertheless, our main objective of the heterostructure design aiming at optical QW transition energies below the band gap of GaAs was successfully achieved.

Figure 7 shows the spectral characteristics of the PL. The spectra were measured with a confocal setup in the central Hall bar region at gate voltages of  $+0.6 \text{ V}$  (flatband condition) for a cw laser excitation wavelength of 830 nm at 4.2 K. The PL exhibits an asymmetric profile reminiscent of Fermi edge singularity [17–19] even at lowest excitation powers down to  $\sim 40 \text{ nW}$  (gray spectrum in Fig. 7). No PL was detected in the relevant spectral window from sample regions where the QW was etched away (blue spectrum in Fig. 7) indicating the QW to be the source of the PL. We find evidence of higher-energy shoulders at 883 and 885 nm that emerge with increasing excitation powers accompanied by a blue-shift of the PL maximum. These characteristics were consistently found at different spatial locations of the Hall bar structure where the QW was not etched away. We also

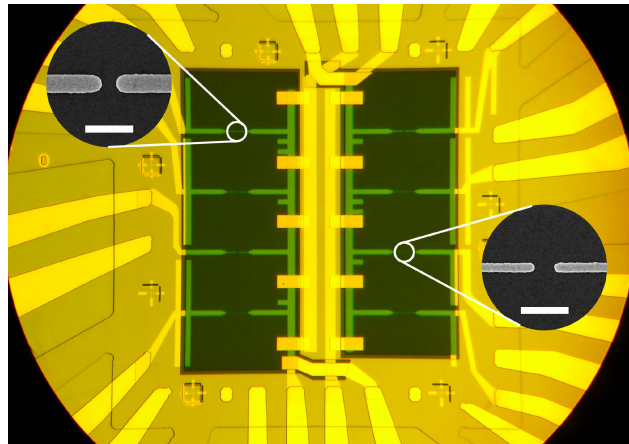


**Figure 8** Optical microscope image of the sample layout with eight QPCs and two global top gates fabricated on the 10 nm InGaAs QW heterostructure. Optical and electron-beam lithography followed by gold deposition and lift-off were used to define gates (yellow) on top of a square mesa with an edge length of  $160 \mu\text{m}$ . The QPCs are formed between the ends of finger-like gates (also shown as scanning-electron micrograph insets each including a horizontal scale bar corresponding to  $1 \mu\text{m}$  length) of different geometries. On the top of the mesa two semitransparent rectangular gates were deposited which are electrically disconnected by cross-linked PMMA from all other gates used to define the QPCs.

found that the PL was sensitive to the gate voltage. The inset of Fig. 7 compares the PL spectra at  $V_i = +0.6$  and  $-2.0 \text{ V}$ , showing a clear blue-shift of the PL resonance with more negative gate voltages that was accompanied by a gradual evolution of the PL line shape toward a symmetric Gaussian peak (fit not shown).

**3.3 Outlook** The basic properties of the heterostructure described above represent a promising starting point for in-detail transport and optical studies of the 0.7-anomaly in QPCs. Figure 8 shows an optical micrograph of our present sample layout implemented on a heterostructure that contains a 2DES hosted by an InGaAs QW of 10 nm thickness. Gold gates defined by optical lithography (outer yellow pads) connect to inner gold gates processed by electron beam lithography (light yellow) across the mesa-edges (centered square and starlike surrounding connections). Eight QPCs of different widths and lengths of the gated constrictions between 200 and 500 nm are covered by layers of cross-linked poly methyl methacrylate (PMMA) (dark gray). The latter electrically isolates the QPC gates from the two semitransparent nickel–chromium top gates of 5 nm thickness (black rectangles on top of the PMMA in Fig. 8). They allow simultaneous optical access to the 2DES layer and tunability of carrier density. The insets in Fig. 8 show SEM pictures of two specific QPC geometries.

Figure 9 shows a series of conductance measurements on a specific QPC of the sample in Fig. 8 as function of the QPC gate voltage and a temperature of 4.2 K. Each pinch-off curve was measured at a top gate voltage  $V_i$  set equidistantly

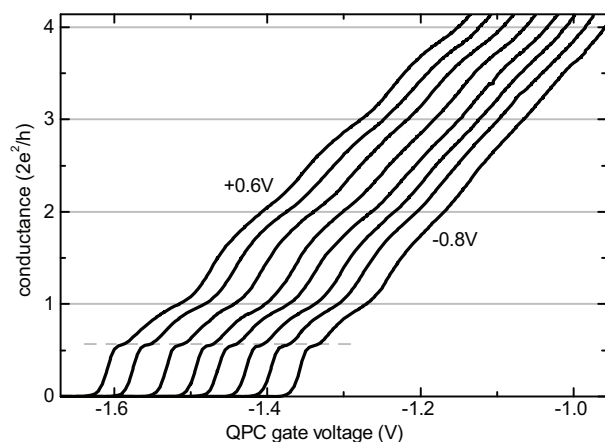


**Figure 9** Conductance through a QPC of the sample in Fig. 8 measured at a setup temperature of 4.2 K. Shown are eight pinch-off curves as function of the QPC gate voltage, at various top gate voltages set between  $-0.8$  and  $+0.6$  V in steps of  $0.2$  V. Integer values of the spin-degenerate conductance quantum are highlighted by gray solid lines. A strongly pronounced kink is consistently visible at around  $0.6 G_Q$  (dashed line).

between  $-0.8$  and  $+0.6$  V. A more positive voltage applied to the extended top gate increases the carrier density in the vicinity of the QPC, which shifts the QPC pinch-off to more negative voltages. Although thermally smeared out, four conductance plateaus are clearly visible at  $V_t = +0.6$  V. Each emerging plateau becomes increasingly pronounced at higher 2DEG densities since the steeper lateral QPC confinement potential barriers raise the sublevel spacing within the constriction region. Additionally, a distinct kink occurs at about  $0.6 G_Q$  throughout the whole top gate voltage range of  $1.4$  V (dashed line in Fig. 9). Its position as well as prominent appearance, compared to the QPC integer conductance plateaus at  $4.2$  K [4, 5], are indications of a  $0.7$ -anomaly.

The next step will involve detailed transport experiments to study the  $0.7$ -anomaly as a function of the QPC geometries in the accessible experimental parameter space. In opto-transport experiments we will then attempt to optically monitor the field dependence of the spin-up and spin-down densities in the vicinity of the QPC as a function of QPC gate voltage  $V_c$  and top gate voltage  $V_t$ . We will also aim to perform near-resonant injection of spin-polarized electrons in the vicinity of a QPC to observe spin-selective transport. We intend to exploit the full potential of the combined optical and transport setup in terms of position, energy and spin selective

spectroscopy to shed light on the microscopic origin of the  $0.7$ -anomaly.

**Acknowledgements** We thank J. P. Kotthaus for helpful discussions. We gratefully acknowledge funding by the Deutsche Forschungsgemeinschaft within the priority program "Semiconductor Spintronics" (SPP 1285) and the center of Excellence, Nanosystems Initiative Munich (NIM) as well as financial support from the Center for NanoScience (CeNS).

## References

- [1] B. J. van Wees, H. van Houten, C. W. J. Beenakker, J. G. Williamson, L. P. Kouwenhoven, D. van der Marel, and C. T. Foxon, *Phys. Rev. Lett.* **60**, 848 (1988).
- [2] D. A. Wharam, T. J. Thornton, R. Newbury, M. Pepper, H. Ahmed, J. E. F. Frost, D. G. Hasko, D. C. Peacock, D. A. Ritchie, and G. A. C. Jones, *J. Phys. C* **21**, L209 (1988).
- [3] M. Büttiker, *Phys. Rev. B* **41**, 7906 (1990).
- [4] K. J. Thomas, J. T. Nicholls, M. Y. Simmons, M. Pepper, D. R. Mace, and D. A. Ritchie, *Phys. Rev. Lett.* **77**, 135 (1996).
- [5] K. J. Thomas, J. T. Nicholls, N. J. Appleyard, M. Y. Simmons, M. Pepper, D. R. Mace, W. R. Tribe, and D. A. Ritchie, *Phys. Rev. B* **58**, 4846 (1998).
- [6] N. J. Appleyard, J. T. Nicholls, M. Pepper, W. R. Tribe, M. Y. Simmons, and D. A. Ritchie, *Phys. Rev. B* **62**, R16275 (2000).
- [7] S. M. Cronenwett, H. J. Lynch, D. Goldhaber-Gordon, L. P. Kouwenhoven, C. M. Marcus, K. Hirose, N. S. Wingreen, and V. Umansky, *Phys. Rev. Lett.* **88**, 226805 (2002).
- [8] A. P. Micolich, *J. Phys.: Condens. Matter* **23**, 443201 (2011).
- [9] F. Bauer, J. Heyder, E. Schubert, D. Borowsky, D. Taubert, B. Bruognolo, D. Schuh, W. Wegscheider, J. von Delft, and S. Ludwig, *Nature* **501**, 73 (2013).
- [10] F. Bauer, J. Heyder, and J. von Delft, *Phys. Rev. B* **89**, 045128 (2014).
- [11] C. Wetterich, *Phys. Lett. B* **301**, 90 (1993).
- [12] W. Metzner, M. Salmhofer, C. Honerkamp, V. Meden, and K. Schönhammer, *Rev. Mod. Phys.* **84**, 299 (2012).
- [13] V. Meden, W. Metzner, U. Schollwöck, and K. Schönhammer, *Phys. Rev. B* **65**, 045318 (2002).
- [14] S. Andergassen, T. Enss, V. Meden, W. Metzner, U. Schollwöck, and K. Schönhammer, *Phys. Rev. B* **70**, 075102 (2004).
- [15] <http://www.nextnano.de/nextnano3>.
- [16] G. B. Stringfellow, W. Koschel, F. Briones, J. Gladstone, and G. Patterson, *Appl. Phys. Lett.* **39**, 581 (1981).
- [17] G. D. Mahan, *Phys. Rev.* **153**, 882 (1967).
- [18] P. Hawrylak, *Phys. Rev. B* **44**, 3821 (1991).
- [19] C. L. Kane, K. A. Matveev, and L. I. Glazman, *Phys. Rev. B* **49**, 2253 (1994).